

Portable Intrinsic Gradiometer for Ultra-Sensitive Detection of Magnetic Gradient in Unshielded Environment

Rui Zhang,^{1,a)} Rahul Mhaskar,²⁾ Ken Smith,¹⁾ and Mark Prouty¹⁾

¹*Geometrics, Inc., San Jose, CA, 95131, USA*

²*formerly Geometrics, Inc., San Jose, CA, 95131, USA, now Keysight Technologies, Santa Clara, 95051, USA*

We demonstrate a portable intrinsic scalar magnetic gradiometer composed of miniaturized cesium vapor cells and vertical-cavity surface-emitting lasers (VCSELs). Two cells, with an inner dimension of 5 mm x 5 mm x 5 mm and separated by 5 cm, are driven by one VCSEL and the resulting Larmor precessions are probed by a second VCSEL through optical rotation. The off-resonant linearly polarized probe light interrogates two cells at the same time and directly reads out the amplitude difference between magnetic fields at two cell locations. The intrinsic gradiometer scheme has the advantage of avoiding added noise from combining two scalar magnetometers. We achieve better than 18 fT/cm/ $\sqrt{\text{Hz}}$ sensitivity in the gradient measurement. Ultra-sensitive short-baseline magnetic gradiometers can potentially play an important role in many practical applications, such as nondestructive evaluation and unexplode ordnance (UXO) detection. Another application of the gradiometer is for magnetocardiography (MCG) in an unshielded environment. Real-time MCG signals can be extracted from the raw gradiometer readings. The intrinsic gradiometer greatly simplifies the MCG setup and may lead to ubiquitous MCG measurement in the future.

Over the last two decades, many breakthroughs have been achieved in atomic magnetometer research. For example, the discovery of the spin-exchange relaxation-free (SERF) phenomenon at high atomic density and low magnetic field leads to a great improvement in the magnetometer noise performance [1]. Sensitivities comparable with [2] or even outperforming [3] those of superconducting quantum interference devices (SQUIDs) have been reported with SERF magnetometers. Another example is the successful fabrication of atomic magnetometers using the technique of Micro-Electro-Mechanical Systems (MEMS) [4, 5, 6, 7, 8]. MEMS techniques enable chip-scale devices, significantly reducing size and power-consumption of atomic magnetometers. Chip-scale magnetometers can have sizes approaching 10 mm³ and dissipate less than 200 mW. Despite all these advances, applications of atomic magnetometers are still limited. Highly sensitive SERF magnetometers require a magnetically shielded environment while chip-scale total-field magnetometers have subpar noise performances [5], although a scalar magnetometer with a sensitivity of 100 fT/ $\sqrt{\text{Hz}}$ has been demonstrated using a MEMS-based cesium vapor cell [9]. With bigger cells, scalar magnetometers can reach sensitivities of sub-10 fT/ $\sqrt{\text{Hz}}$ [10] or even sub-fT/ $\sqrt{\text{Hz}}$ [11]. In practical applications in an unshielded environment, the output noise of scalar magnetometers is often dominated by the background field fluctuation, instead of their fundamental sensitivities. To overcome this problem, a common solution is to set up a gradiometer system using two or more magnetometers [12, 13, 14]. By taking the reading difference between adjacent magnetometers, this conventional gradiometer configuration suppresses the common field fluctuations at the cost of worsening the fundamental sensitivity by at least a factor of $\sqrt{2}$, compared with that of an individual magnetometer. Here, we describe an intrinsic scalar gradiometer scheme that reads out the magnetic gradient optically and thus avoids the reduced sensitivity issue with the conventional gradiometer. In addition, we built a portable device based on the intrinsic gradiometer scheme, using miniaturized cesium vapor cells and vertical-cavity surface-emitting lasers (VCSELs), two components essential for compact and low-power devices. We demonstrate a gradiometer output noise density of less than 90 fT/ $\sqrt{\text{Hz}}$, which is equivalent to 18 fT/cm/ $\sqrt{\text{Hz}}$ sensitivity in the gradient measurement for a baseline of 5 cm. A similar sensitivity is expected for a proposed atomic magnetometer system [15] and a slightly better sensitivity was achieved with a portable gradiometer using two scalar magnetometers recently [16].

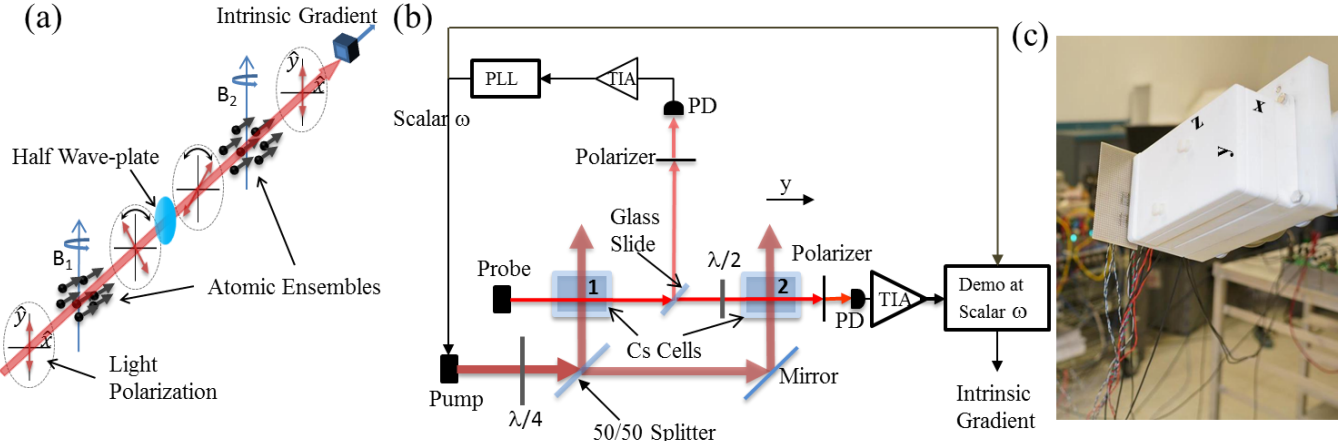


Figure 1 (a) Basic principle of the intrinsic gradiometer. (b) Schematic of implementing the intrinsic gradiometer. (c) Portable device based on the intrinsic gradiometer scheme. The device has a dimension of 5 cm x 10 cm x 15 cm along x, y and z, respectively.

The basic principle of the intrinsic gradiometer is illustrated in Figure 1 (a). A single linearly-polarized off-resonant probe interrogates two atomic ensembles separated by a baseline distance. The atoms at both locations are spin-polarized exactly the same way. After interacting with the first atomic ensemble, the probe goes through a half-wave plate oriented such that the acquired polarization rotation of the probe beam is reversed. If the magnetic fields at the two locations are exactly the same, the second ensemble of atoms rotates the probe polarization back to its original position. The optical rotation effect is cancelled. However, if there is a magnetic field gradient, the difference in precession frequencies will result in non-cancellation in the rotation of the probe polarization. Therefore, the probe polarization signal is a direct measurement of the magnetic field gradient. Detailed description of the sensor will be published in the future [17].

The intrinsic gradiometer can be realized schematically shown in Figure 1 (b). Light from the pump VCSEL is circularly polarized and then equally split into two beams, exciting cesium atoms at two vapor cells. A linearly polarized off-resonant beam from the probe VCSEL interacts with the two atomic ensembles at the same time. About 10% light is split from the main probe beam by a piece of glass slide and is detected by a photodiode after an analyzing linear polarizer. The photodiode current is then amplified and sent to a phase-lock-loop (PLL) circuit. The output of the PLL drives the pump laser through current modulation and is the scalar measurement of the magnetic field at the first cell. After the second cell, the main probe beam is analyzed by a linear polarizer and detected by a photodiode, whose current is amplified and sent to a demodulator with its reference frequency determined by the PLL output. The quadrature component of the demodulated probe signal is converted to the intrinsic gradiometer reading with a constant determined by the slope of the quadrature component at the magnetic resonance.

We built a portable gradiometer by housing all optics and VCSELs inside a 3D printed structure, as shown in Figure 1 (c). The sensor head has a dimension of 5 cm x 10 cm x 15 cm in x, y and z directions, respectively. Two cesium vapor cells with 60 Torr N₂ buffer gas and an inner dimension of 5 mm x 5mm x 5mm are separated by 5 cm along the y direction. Two VCSEL packages, photodiodes and their transimpedance amplifier circuits are integrated on a printed circuit board (PCB), which is mounted on the far side of the sensor head in the z direction. The cells are placed 14 cm away from the PCB to avoid the magnetic contamination from the electronics. With customized non-magnetic electrical components, it is straight forward to reduce the sensor size to 3 cm x 6 cm x 3 cm. In operation, the pump VCSEL laser is resonant on the |F=3> → |F'=4> transition of the cesium D1 line and its current is modulated by the PLL output. The pump beam has a total power of 350 μW. The probe VCSEL is 15 GHz red detuned with respect to the |F=4> → |F'=3> transition of the cesium D1 line with 150 μW in power. Both lasers have a Gaussian spatial profile with FWHM of about 1.8 mm. The vapor cells are heated to 68°C.

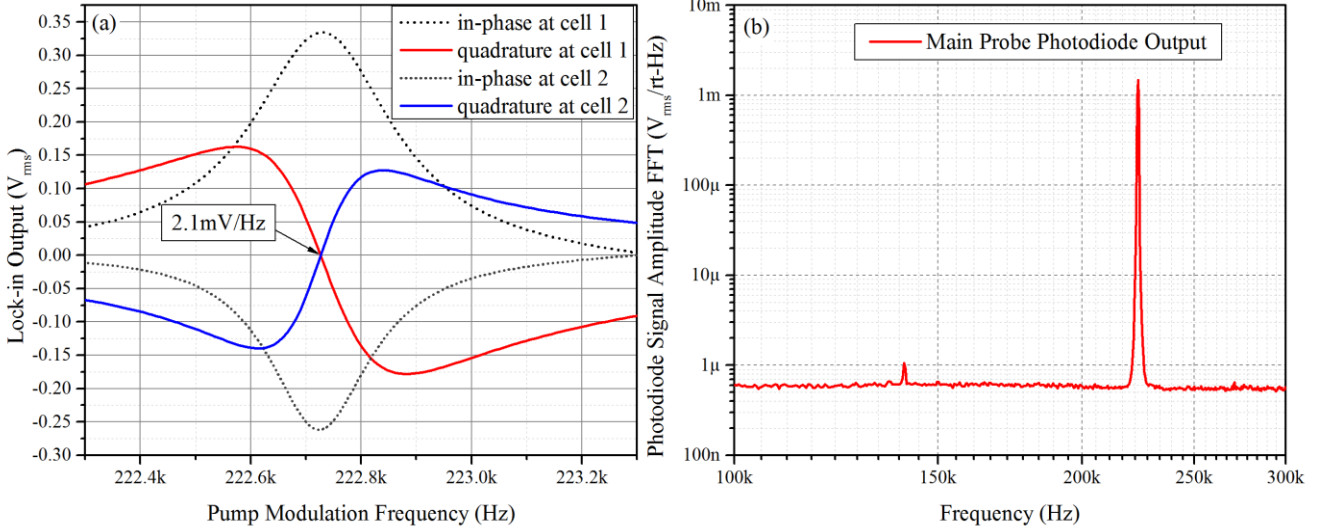


Figure 2 (a) Main probe lock-in signal as a function of pump modulation frequency f . The black dot (red and blue solid) curves represent the in-phase (quadrature) components at two cells. (b) Amplitude spectral density of the main probe photodiode signal after the transimpedance amplifier.

We first test the gradiometer inside a shield can with the background magnetic field set at 63,600 nT. Magnetic resonance at an individual cell can be measured by demodulating the main probe signal at the pump modulation frequency while blocking the pump beam exciting the other cell. Both the in-phase and the quadrature components at two cells are shown in Figure 2 (a). As seen, the precession signals at the two cells are exactly opposite in phase. The cell temperatures are adjusted to optimize and match the slopes of the two quadrature components at the magnetic resonance frequency. The slope is $k = 2.1$ mV/Hz. We also measure the main probe photodiode noise spectral density, $d \approx 550$ nV/ $\sqrt{\text{Hz}}$, as shown in Figure 2 (b). The fundamental individual magnetometer noise density can be estimated as $d/(k^*\gamma) \approx 75$ fT/ $\sqrt{\text{Hz}}$, where $\gamma \approx 3.5\text{Hz/nT}$ is the gyromagnetic ratio of cesium atoms. The intrinsic gradiometer noise is the same as that of the individual magnetometer as long as the gradient is much smaller than the width of the magnetic resonance. Similarly, the scalar magnetometer using the split probe beam is estimated to have a fundamental sensitivity of 300 fT/ $\sqrt{\text{Hz}}$.

The fundamental sensitivity of atomic magnetometers is often limited by the photon shot noise, which is given by $\sqrt{2hvp}$, where $h\nu$ is the single photon energy and p is the total light power. After the linear polarizer, the main probe power is reduced to 26 μW . With $\lambda = 895$ nm, photodiode efficiency of 0.65 A/W and 200 k Ω transimpedance amplifier gain, the spectral density of the main probe photodiode signal due to the photon shot noise is 440 nV/ $\sqrt{\text{Hz}}$, which is close to the measured value at 550 nV/ $\sqrt{\text{Hz}}$. This indicates that the sensor operates close to the photon-shot-noise limit.

The scalar magnetometer based on the split probe beam operates in the closed-loop mode and measures the magnetic field at the first cell. The main probe signal, carrying the gradient information, is demodulated by the scalar magnetometer output frequency. The phase of the demodulator is set to be the same as that of the PLL for the split probe signal. The quadrature output of the demodulator is converted directly to the gradient by multiplying a constant given by $1/(k^*\gamma) \approx 0.1361$ nT/mV. The gradiometer output is essentially the combined signal of the two quadrature components, as shown in Figure 2 (a), at a certain pump modulation frequency determined by the scalar magnetometer. The gradiometer sensitivity is not affected by the fundamental noise of the scalar magnetometer, which is equivalent to a small fluctuation of the pump modulation frequency around the actual magnetic resonance frequency. As seen in Figure 2 (a), as long as the slopes match, two quadrature components still cancel each other even when the pump modulation frequency fluctuates. The better the slopes match, the less affected the gradiometer sensitivity is by the fundamental noise of the scalar magnetometer.

The noise densities, averaged for 6 minutes, of both the scalar magnetometer (red) and the intrinsic gradiometer (green) are shown in Figure 3. As seen, the scalar output noise density is 300 fT/ $\sqrt{\text{Hz}}$, exactly as expected while the gradiometer noise density is below 90 fT/ $\sqrt{\text{Hz}}$, which is close to the estimated noise density of 75 fT/ $\sqrt{\text{Hz}}$. The extra gradient noise may be due to the magnetic shield [18] since the vapor cells are only 5 cm away from the shielding metal due to the limited size of the

shield can. Even at $90 \text{ fT}/\sqrt{\text{Hz}}$, the demonstrated noise clearly indicates the advantage of the intrinsic gradiometer scheme since the conventional gradiometer configuration with two $75 \text{ fT}/\sqrt{\text{Hz}}$ scalar magnetometers cannot have a gradient noise better than $106 \text{ fT}/\sqrt{\text{Hz}}$. The accuracy of the gradient conversion constant is verified by a 20 Hz testing signal. The signal is generated by a 3 mm diameter coil attached to the first cell. Due to the size of the coil and the distance between the coil and the second cell, the signal is almost negligible at the second cell. Therefore, the 20 Hz signal measured by the intrinsic gradiometer should have the same amplitude as that measured by the scalar magnetometer if the conversion constant is accurate, which is confirmed as shown in Figure 3. By sending fixed amplitude signals at different frequencies through the same 3 mm coil, the 3-dB bandwidth of the scalar magnetometer and the intrinsic gradiometer is measured to be 300 Hz and 150 Hz, respectively. The bandwidth data is plotted in the inset of Figure 3.

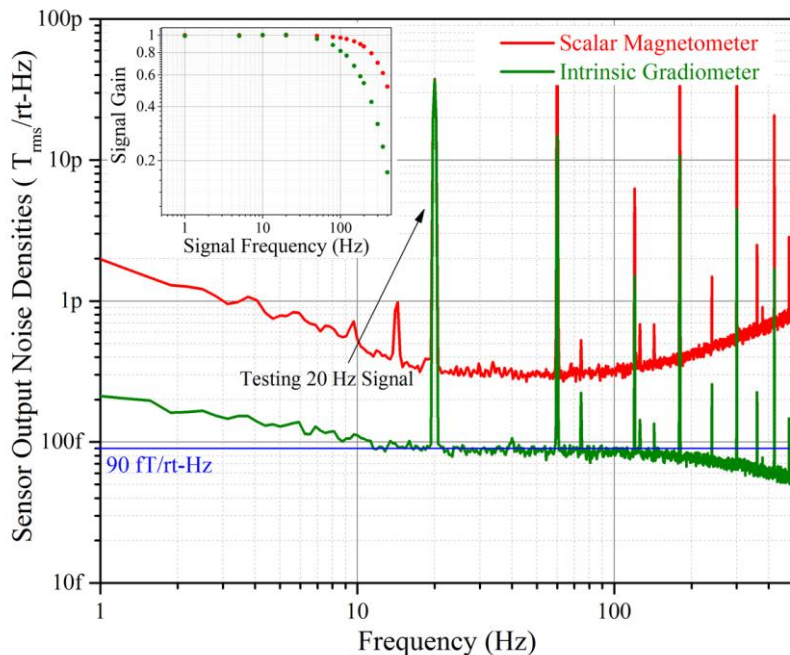


Figure 3 Noise densities of the scalar magnetometer (red) and the intrinsic gradiometer (green) inside a shield can. The inset shows their bandwidths.

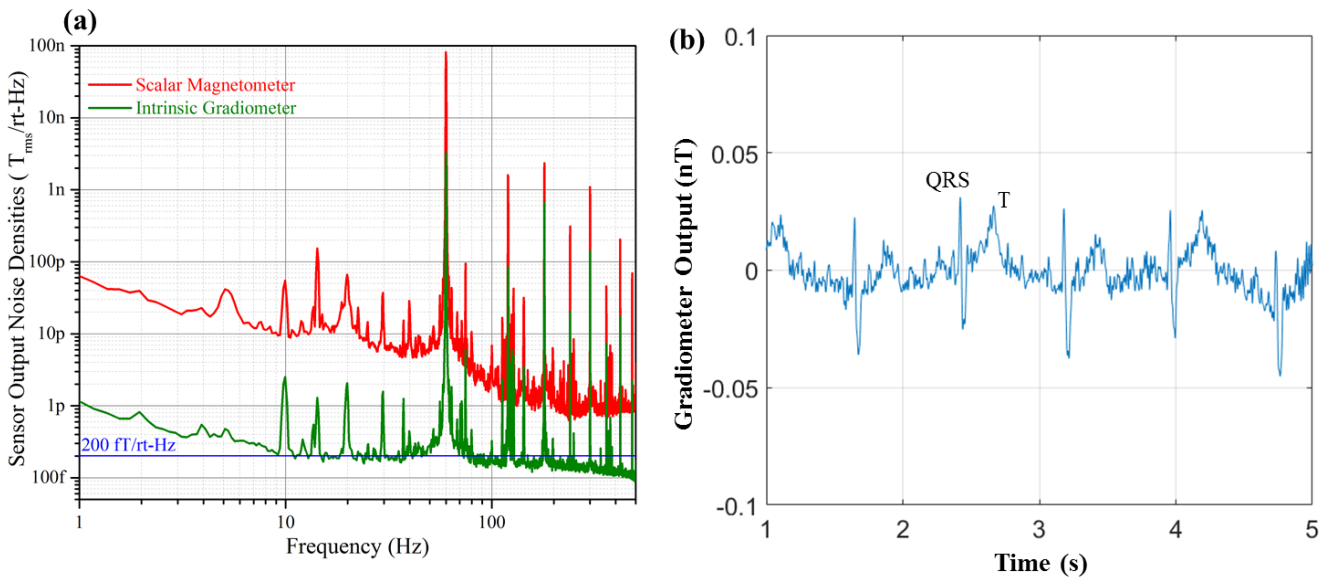


Figure 4 (a) Noise densities of the scalar magnetometer (red) and the intrinsic gradiometer (green) in an unshielded environment. (b) Real-time MCG data with 60 Hz notch filter and 70 Hz low-pass filter.

Taking into account the 5 cm separation between the two cells, the gradiometer sensitivity is better than 18 fT/cm/ $\sqrt{\text{Hz}}$. Combined with the bandwidth of over 100 Hz, the intrinsic gradiometer can be used for many applications such as nondestructive evaluation [19], unexplode ordnance (UXO) detection [20] and magnetocardiography (MCG) in an unshielded environment [21, 22, 23, 24]. Here we demonstrate the MCG application in an office environment. The setup is shown in Figure 1 (c). The noise density in the unshielded environment is first measured and plotted in Figure 4 (a). The gradiometer noise is worse compared with that in the magnetic shield due to the real gradient fluctuation inside a commercial building. From the noise density plot, it is also obvious that we need to remove the 60 Hz power line noise and its harmonics, which is done by a 60 Hz notch filter and a 70 Hz low-pass filter. The MCG data is recorded when a person is standing by the gradiometer with his chest 2 cm away from the second cell. After the two filters, the gradiometer output is shown in Figure 4 (b). As seen, even in a very magnetically noisy office environment, real-time MCG signals are clearly visible.

In conclusion, we demonstrate a portable intrinsic gradiometer that can be operated in unshielded environments. By using miniaturized vapor cells and VCSEL lasers, we show the feasibility of an ultra-sensitive magnetic gradiometer in a highly compact physics package. Combined with the all-optical operation to avoid the interference between nearby devices, such a sensor can be built into arrays for fast data collection and further magnetic noise suppression. For applications involving mobile platforms, such as UXO detection, more research efforts are necessary to study heading error effects. One of the main issues of the current gradiometer scheme is the dependence of the gradient conversion constant on the relative orientation between the sensor and the background magnetic field, causing a large heading error. In principle this heading error can be minimized by introducing an automatic gain based the amplitude of the input precession signal. As long as the quality factor of the magnetic resonance remains the same, the conversion constant will not change. On the other hand, we believe that this work eliminates major challenges of applying atomic magnetometers for stationary applications, such as MCG in unshielded environments. Development of commercially available intrinsic gradiometers can definitely advance the MCG research and may lead to ubiquitous MCG measurement in the future.

The data that support the findings of this study are available from the corresponding author upon reasonable request.

The authors would like to thank Mehdi Malek and Ken Glasser for their help in designing the 3D gradiometer housing and Lynn Edwards for his work on setting up testing fixtures. This work is supported by Strategic Environmental Research and Development Program (SERDP) under project number MR19-1379. The views expressed are those of the authors and should not be interpreted as representing the official views of the Department of Defense or the U.S. Government.

Bibliography

- [1] J. C. Allred, R. N. Lyman, T. W. Kornack and M. V. Romalis, "High-sensitivity atomic magnetometer unaffected by spin-exchange relaxation," *Phys. Rev. Lett.*, vol. 89, p. 130801, 2002.
- [2] I. K. Kominis, T. W. Kornack, J. C. Allred and M. V. Romalis, "A subfemtotesla multichannel atomic magnetometer," *Nature*, vol. 422, pp. 596-599, 2003.
- [3] H. B. Dang, A. C. Maloof and M. V. Romalis, "Ultrahigh sensitivity magnetic field and magnetization measurements with an atomic magnetometer," *Appl. Phys. Lett.*, vol. 97, no. 15, p. 151110, 2010.
- [4] P. D. D. Schwindt, S. Knappe, V. Shah, L. Hollberg and J. Kitching, "Chip-scale atomic magnetometer," *Appl. Phys. Lett.*, vol. 85, no. 26, p. 6409, 2004.
- [5] P. D. D. Schwindt, B. Lindseth, S. Knappe, V. Shah and J. Kitching, "Chip-scale atomic magnetometer with improved sensitivity by use of the Mx technique," *Appl. Phys. Lett.*, vol. 90, no. 8, p. 081102, 2007.
- [6] R. Mhaskar, S. Knappe and J. Kitching, "A low-power, high-sensitivity micromachined optical magnetometer," *Appl. Phys. Lett.*, vol. 101, no. 24, p. 241105, 2012.
- [7] S. Knappe, O. Alem, D. Sheng and J. Kitching, "Microfabricated Optically-Pumped Magnetometers for Biomagnetic Applications," *Journal of Physics: Conference Series*, vol. 723, p. 012055, 2016.
- [8] J. Kitching, "Chip-scale atomic devices," *Applied Physics Reviews*, vol. 5, p. 031302, 2018.
- [9] R. Zhang, T. Dyer, N. Brockie, R. Parsa and R. Mhaskar, "Subpicotesla scalar atomic magnetometer with a microfabricated cell," *Journal of Applied Physics*, vol. 126, no. 12, p. 124503, 2019.
- [10] S. J. Smullin, I. M. Savukov, G. Vasilakis, R. K. Ghosh and M. V. Romalis, "Low-noise high-density alkali-metal scalar magnetometer," *Phys. Rev. A*, vol. 80, no. 3, p. 033420, 2009.
- [11] D. Sheng, S. Li, N. Dural and M. V. Romalis, "Subfemtotesla Scalar Atomic Magnetometry Using Multipass Cells," *Phys. Rev. Lett.*, vol. 110, no. 16, p. 160802, 2013.

- [12] C. Affolderbach, M. Stahler, S. Knappe and R. Wynands, "An all-optical, high-sensitivity magnetic gradiometer," *Applied Physics B*, vol. 75, p. 605, 2002.
- [13] G. Bevilacqua, V. Biancalana, P. Chessa and Y. Dancheva, "Multichannel optical atomic magnetometer operating in unshielded environment," *Applied Physics B*, vol. 122, p. 103, 2016.
- [14] V. G. Lucivero, W. Lee, M. E. Limes, E. L. Foley, T. W. Kornack and M. V. Romalis, "A femtotesla quantum-noise-limited pulsed gradiometer at finite fields," *Quantum Information and Measurement*, p. T3C.3, 2019.
- [15] M. D. Bulatowicz, T. G. Walker and M. S. Larsen, "Pulsed-beam atomic magnetometer system". United States of America Patent US20180372813A1, 27 12 2018.
- [16] M. E. Limes, E. L. Foley, T. W. Kornack, S. Caliga, S. McBride, A. Braun, W. Lee, V. G. Lucivero and M. V. Romalis, "Total-field atomic gradiometer for unshielded portable magnetoencephalography," *arXiv*, p. 2001.03534, 2020.
- [17] R. Zhang, "Intrinsic Scalar Magnetic Gradiometer for Accurate Localization of Magnetic Anomalies," SERDP project MR19-1739, 2020.
- [18] S.-K. Lee and M. V. Romalis, "Calculation of magnetic field noise from high-permeability magnetic shields and conducting objects with simple geometry," *Journal of Applied Physics*, vol. 103, p. 084904, 2008.
- [19] Y. Watanabe, S. H. Kang, J. W. Chan, J. W. Morris, T. J. Shaw and J. Clarke, "Observation of magnetic gradients in stainless steel with a high-T_c superconducting quantum interference device microscope," *Journal of Applied Physics*, vol. 89, p. 1977, 2001.
- [20] A. Salem, T. Hamada, J. K. Asahina and K. Ushijima, "Detection of unexploded ordnance (UXO) using marine magnetic gradiometer data," *Exploration Geophysics*, vol. 36, pp. 97-103, 2005.
- [21] G. Bison, R. Wynands and A. Weis, "A laser-pumped magnetometer for the mapping of human cardiomagnetic fields," *Applied Physics B*, vol. 76, no. 3, p. 325, 2003.
- [22] R. Wyllie, M. Kauer, R. T. Wakai and T. G. Walker, "Optical magnetometer array for fetal magnetocardiography," *Optics Letters*, vol. 37, no. 12, p. 2247, 2012.
- [23] O. Alem, T. H. Sander, R. Mhaskar, J. LeBlanc, H. Eswaran, U. Steinhoff, Y. Okada, J. Kitching, L. Trahms and S. Knappe, "Fetal magnetocardiography measurements with an array of microfabricated optically pumped magnetometers," *Physics in Medicine & Biology*, vol. 60, p. 4797, 2015.
- [24] M. Bai, Y. Huang, G. Zhang, W. Zheng, Q. Lin and Z. Hu, "Fast backward singular value decomposition (SVD) algorithm for magnetocardiographic signal reconstruction from pulsed atomic magnetometer data," *Optics Express*, vol. 27, no. 21, p. 29534, 2019.